



Direct observation of ligand migration within human hemoglobin at work

Naoya Shibayama^{a,1} , Ayana Sato-Tomita^a, Mio Ohki^b, Kouhei Ichiyanagi^a, and Sam-Yong Park^c

^aDivision of Biophysics, Department of Physiology, Jichi Medical University, Tochigi, 329-0498 Shimotsuke, Japan; ^bResearch Complex at Harwell, Rutherford Appleton Laboratory, Harwell, Didcot, Oxon OX11 0FA, United Kingdom; and ^cDrug Design Laboratory, Graduate School of Medical Life Science, Yokohama City University, Tsurumi, 230-0045 Yokohama, Japan

Edited by William A. Eaton, National Institute of Diabetes and Digestive and Kidney Diseases, Bethesda, MD, and approved January 24, 2020 (received for review August 8, 2019)

Hemoglobin is one of the best-characterized proteins with respect to structure and function, but the internal ligand diffusion pathways remain obscure and controversial. Here we captured the CO migration processes in the tense (T), relaxed (R), and second relaxed (R2) quaternary structures of human hemoglobin by crystallography using a high-repetition pulsed laser technique at cryogenic temperatures. We found that in each quaternary structure, the photodissociated CO molecules migrate along distinct pathways in the α and β subunits by hopping between the internal cavities with correlated side chain motions of large nonpolar residues, such as α 14Trp(A12), α 105Leu(G12), β 15Trp(A12), and β 71Phe(E15). We also observe electron density evidence for the distal histidine [α 58/ β 63His(E7)] swing-out motion regardless of the quaternary structure, although less evident in α subunits than in β subunits, suggesting that some CO molecules have escaped directly through the E7 gate. Remarkably, in T-state Fe(II)-Ni(II) hybrid hemoglobins in which either the α or β subunits contain Ni(II) heme that cannot bind CO, the photodissociated CO molecules not only dock at the cavities in the original Fe(II) subunit, but also escape from the protein matrix and enter the cavities in the adjacent Ni(II) subunit even at 95 K, demonstrating the high gas permeability and porosity of the hemoglobin molecule. Our results provide a comprehensive picture of ligand movements in hemoglobin and highlight the relevance of cavities, nonpolar residues, and distal histidines in facilitating the ligand migration.

hemoglobin | ligand migration | X-ray crystallography | allostery

Human hemoglobin (Hb), an $\alpha_2\beta_2$ tetrameric oxygen transport protein that binds gaseous ligands such as O₂ and CO cooperatively at the four heme irons, serves as a model for studying protein–ligand interactions (Fig. 1A). After the pioneering work by Perutz (1), the mechanisms of Hb and its reaction with ligands have been explained based on the crystal structures of the deoxy tense (T) and fully liganded relaxed (R) quaternary states (2–5). However, a fundamental question still under debate concerns the pathways for ligands from the solvent to the heme iron, since crystal structures display no obvious gas channels leading to the heme sites (Fig. 1B).

Previous crystallographic analysis of T-state deoxy Hb under pressurized Xe identified the positions of Xe binding cavities in the α and β subunits (Fig. 1C and D) (6). Four are located in α , labeled α Xe1, α Xe2, α Xe3, and α Xe6, and two are in β , labeled β Xe1 and β Xe2, using the same nomenclature as in the previous study (6). It was suggested that these internal cavities may play a role as transient areas for ligands migrating through the protein interior in both subunits of human Hb. In support of this idea, recent molecular dynamics (MD) simulations have demonstrated that kinetically accessible ligand diffusion tunnels in Hb encompass the reported Xe cavities regardless of the quaternary structure (7, 8). On the other hand, however, experimental data on CO rebinding kinetics after photolysis of distal pocket mutants of Hb bound to CO (COHb) do not support this idea, but instead suggest that most ligands enter and escape directly through the distal

His(E7) gate pathway (9, 10). Therefore, controversy remains as to whether the Xe-binding cavities play a functional role in Hb.

For directly observing the ligand migration in Hb, X-ray crystallographic analysis of COHb after photolysis is obviously preferred but is quite challenging and complex, due to the relatively low apparent quantum yield for the photolysis of COHb (11), as well as the need to address the quaternary structure dependence of gas diffusion as predicted by MD simulations (7). In addition, excitation light transfer to the sample, together with the rapid kinetics of CO recombination, place limits on crystal thickness and measurement temperature. To date, only two crystallographic approaches have been reported on this topic for Hb. One is a cryogenic approach to increase the level of CO photolysis by lowering the temperature to 25 to 35 K, where CO rebinding is very slow and virtually negligible during the measurement (12). It has been shown that continuous illumination of crystals of the T and R states of human Hb allows a high level of CO photolysis, but most of the photodissociated CO molecules reside at the primary docking site (located \sim 3.5 Å from the iron) within the distal heme pocket (DP), with the exception of a weak CO electron density present in β Xe2 (located \sim 8.5 Å from the iron) in the T state (12). While near-liquid helium temperatures

Significance

Human hemoglobin is the textbook example of the stereochemistry of an allosteric protein and of the exquisite control that a protein can exert over ligand binding. However, the fundamental basis by which the protein facilitates the ligand movement remains unknown. In this study, we used cryogenic X-ray crystallography and a high-repetition pulsed laser irradiation technique to elucidate the atomic details of ligand migration processes in hemoglobin after photolysis of the bound CO. Our data clarify the distinct CO migration pathways in the individual subunits of hemoglobin and unravel the functional roles of the internal cavities and neighboring amino acid residues in ligand exit and entry. Our results also demonstrate the high gas permeability and porosity of hemoglobin, facilitating O₂ delivery.

Author contributions: N.S. designed research; N.S., A.S.-T., M.O., K.I., and S.-Y.P. performed research; N.S. provided sample preparation and crystallization; N.S., A.S.-T., M.O., and S.-Y.P. analyzed data; and N.S. wrote the paper.

The authors declare no competing interest.

This article is a PNAS Direct Submission.

This open access article is distributed under [Creative Commons Attribution-NonCommercial-NoDerivatives License 4.0 \(CC BY-NC-ND\)](https://creativecommons.org/licenses/by-nc-nd/4.0/).

Data deposition: The atomic coordinates and structure factors have been deposited in the Protein Data Bank, <https://www.wwpdb.org/> (PDB ID codes 6KA9, 6KAE, 6KAH, 6KAI, 6KAO, 6KAP, 6KAQ, 6KAR, 6KAS, 6KAT, 6KAU, 6KAV, 6LSV, 6LSW, 6LSX, 6LSY, 6LCW, and 6LCX).

¹To whom correspondence may be addressed. Email: shibayam@jichi.ac.jp.

This article contains supporting information online at <https://www.pnas.org/lookup/suppl/doi:10.1073/pnas.1913663117/-DCSupplemental>.

First published February 18, 2020.

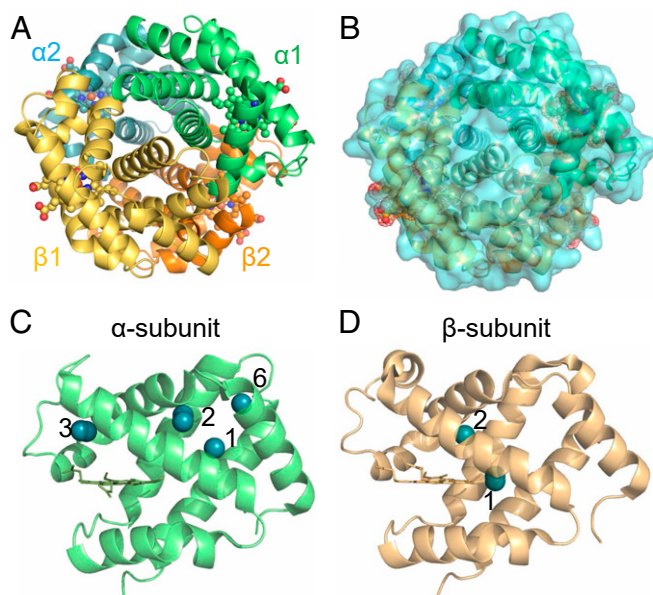


Fig. 1. Structure of Hb. (A) Crystal structure of COHb, with protein backbones shown as ribbons and hemes shown as ball and stick models. (B) The same structure as in A but represented as both surface and ribbons. (C and D) Comparison of Xe-binding cavities in α (C) and β (D) subunits of Hb. Xe's are represented as spheres and labeled by the numbers used in Savino et al. (6).

are beneficial for impeding CO rebinding by decreasing the energy of CO, they also impede migration of the CO from the DP, as previously reported for myoglobin (Mb) (13, 14).

The second approach is the use of room temperature (288 K) time-resolved Laue crystallography to track the structural evolution of R-state COHb at a set of time delays between the pump laser pulse and the probe X-ray pulse (i.e., 100 ps, 1 ns, 10 ns, 100 ns, 1 μ s, and 10 μ s) (15). Although ligand migration and protein relaxation are expected to occur at room temperature, the experiment incurred the problem of a rather small amount of dissociated CO even at 100 ps after the pulse laser irradiation. To deal with this problem, a dataset corresponding to a hypothetical fully photolyzed crystal was calculated by linear extrapolation of structure-factor amplitudes using the scalar approximation. Specifically, the measured structure-factor amplitudes were extrapolated to 100% photolysis by assuming a photolysis level of 15%, where bound CO vanished from the extrapolated maps for both α and β subunits by visual assessment. The generated 100-ps maps showed that the dissociated CO molecules moved 1.5 to 2.0 \AA away from the iron toward the primary docking site. However, no electron density of the CO was found in any other locations within the protein throughout the measurement period, which is inconsistent with the MD simulations. Clearly, there remains a considerable need for additional investigation on Hb.

In this study, we used a high-repetition (10 kHz) 1.2-ns-pulsed 532-nm Nd:YAG laser at a temperature range of 95 to 140 K, where the photodissociated CO overcomes the initial energy barrier and gradually migrates from the DP to more remote cavities in the protein during repeating dissociation and geminate recombination (16, 17). We also use crystals of the T, R, and R2 quaternary states of human Hb to explore the effect of quaternary structure on ligand migration. Note that the structural differences between R and R2 are as large as those between R and T, and that recent MD simulations suggest that ligand escape pathways vary somewhat among T, R, and R2 (7).

Results and Discussion

T-State Crystals of CO-Bound Fe(II)-Ni(II) Hybrid Hbs. We first investigated the CO migration process in the T quaternary structure of human Hb using crystals of two symmetric CO-bound Fe(II)-Ni(II) hybrid Hbs, $\text{XL}[\alpha(\text{Fe-CO})\beta(\text{Ni})]_2$ and $\text{XL}[\alpha(\text{Ni})\beta(\text{Fe-CO})]_2$, in which either the α or β subunits contain Ni(II) heme and the two $\alpha\beta$ dimers are cross-linked by a fumaryl group between the two $\beta 82\text{Lys}(\text{EF6})$ residues. It has been shown that these doubly CO-liganded hybrids yield well-diffracting, optically thin isomorphous T-state crystals (12). It has also already been established that Ni(II)-heme binds neither O_2 nor CO and mimics the deoxy Fe(II)-heme with respect to the effects on the functional properties of the adjacent Fe(II) subunits in the same protein (18, 19), and that the β - β fumaryl cross-link between the two $\beta 82\text{Lys}(\text{EF6})$ residues has little affect on the structure and function of Hb (20).

The X-ray diffraction datasets for the T-state crystals of $\text{XL}[\alpha(\text{Fe-CO})\beta(\text{Ni})]_2$ and $\text{XL}[\alpha(\text{Ni})\beta(\text{Fe-CO})]_2$ were collected in a 95 K nitrogen gas stream under continuous irradiation by 10-kHz pulsed laser light with an average power density of 47 mWmm^{-2} , along with control datasets on the CO-bound states without laser irradiation (SI Appendix, Table S1). Both crystals diffracted to 1.40- to 1.45- \AA resolution with (light) and without (dark) laser irradiation, although relatively small crystals of 15 to 30 μm thickness were used for light transfer. The $2F_{\text{obs}} - F_{\text{calc}}$ electron density maps around the α and β hemes in the dark and light structures at 95 K without (dark) and with (light) laser irradiation of 60 min demonstrate the initially bound CO and the achievement of nearly full photolysis, respectively (Fig. 2). Interestingly, in the α subunits, a detectable amount of CO exists in the primary docking site within the DP (located $\sim 2.9 \text{ \AA}$ from the iron) after photolysis, whereas in the β subunits, a smaller amount of CO remains in the DP. This is consistent with the time-resolved Laue crystallographic data showing much faster CO escape from βDP than from αDP on photolysis (15), and is in line with the MD simulations indicating a smaller relative population of photolyzed ligand in βDP than in αDP (7).

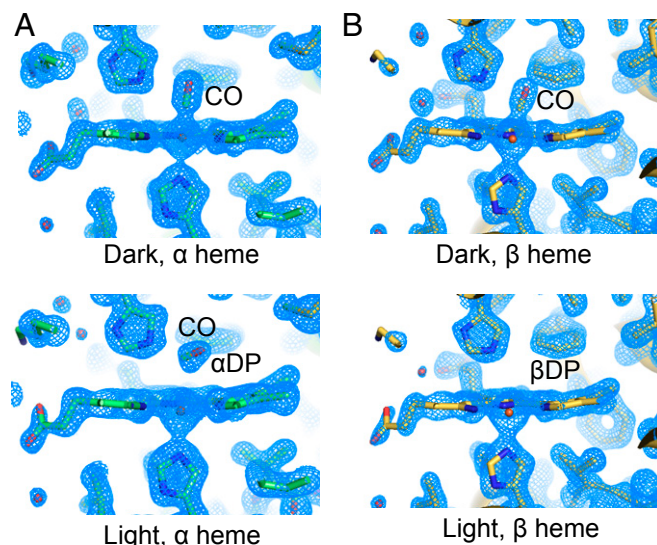


Fig. 2. The refined $2F_{\text{obs}} - F_{\text{calc}}$ electron density maps contoured at 1.5σ (0.7 e/\AA^3 peak density as blue mesh) for the areas around T-state α heme in $\text{XL}[\alpha(\text{Fe-CO})\beta(\text{Ni})]_2$ (A) and T-state β heme in $\text{XL}[\alpha(\text{Ni})\beta(\text{Fe-CO})]_2$ (B) at 95 K without (dark) and with (light) laser irradiation of 60 min. In A and B, the dark (Upper) and light (Lower) structures are seen to demonstrate nearly full photolysis of each heme site. Full data collection and refinement statistics are summarized in SI Appendix, Table S1.

The CO migration and the protein structural changes associated with photolysis are more clearly seen in the $|F_{\text{obs}}^{\text{light}} - |F_{\text{obs}}^{\text{dark}}|$ difference Fourier electron density maps obtained from the same set of crystals (Fig. 3). The maps contoured at $\pm 3.5\sigma$ confirm the loss of bound CO, the out-of-plane motion of the iron toward the proximal side, and the movement of the distal histidine $\alpha 58/\beta 63\text{His}(E7)$ toward the site previously occupied by CO in both Fe(II) subunits (Fig. 3 *A* and *D*). The concomitant movement of the F-helix is more significant in $\alpha(\text{Fe})$ subunits than in $\beta(\text{Fe})$ subunits. Moreover, the β heme undergoes a deligation-linked sliding from pyrrole C to B. These observations are in line with the photolysis-induced structural changes observed at 25 K (12). A marked difference between the light structures at 25 K and 95 K is found in the location of CO. In contrast to the observations at 25 K, at 95 K, positive electron density features corresponding to the dissociated CO molecules are clearly visible in the internal Xe-binding cavities in both subunits (Fig. 3).

CO Migration in $\alpha(\text{Fe})$ Subunits in the T State. In $\text{XL}[\alpha(\text{Fe-CO})\beta(\text{Ni})]_2$, in addition to the electron density of the photodissociated CO remaining in αDP as mentioned above (*SI Appendix, Fig. S1A*), a strong electron density feature definitely corresponding to CO is observed in $\alpha\text{Xe}2$ among helices A, B, E, and G (Fig. 3*A* and see Fig. 1*C*), surrounded by hydrophobic amino acid residues, such as $\alpha 14\text{Trp}(A12)$, $\alpha 17\text{Val}(A15)$, $\alpha 21\text{Ala}(B2)$, $\alpha 24\text{Tyr}(B5)$, and $\alpha 109\text{Leu}(G16)$. This site is relatively close to the solvent and is not shielded by the other subunits of the tetramer. Concomitantly with the appearance of CO, the side chains of $\alpha 14\text{Trp}(A12)$ and $\alpha 105\text{Leu}(G12)$ move in the direction of $\alpha\text{Xe}1$ as a result of a collision of CO (Fig. 3*A*). In addition, a relatively weak electron density feature of CO appears in $\alpha\text{Xe}1$ (Fig. 3*A*). According to the displacement of $\alpha 14\text{Trp}(A12)$, the side chain

distance between $\alpha 14\text{Trp}(A12)$ and $\alpha 17\text{Val}(A15)$ expands to form a transient channel for escape of CO to the solvent. These observations strongly suggest that a likely pathway for CO migration within T-state α subunits is $\text{DP} \rightarrow \alpha\text{Xe}2 \rightarrow \text{solvent}$. This pathway is consistent with a recent MD study on O_2 migration within human Hb, showing that a high percentage of ligand molecules escape via $\alpha\text{Xe}2$ in both T and R (7, 8).

Unexpectedly, we find that in $\text{XL}[\alpha(\text{Fe-CO})\beta(\text{Ni})]_2$ the dissociated CO molecules not only dock at the cavities in the original $\alpha(\text{Fe-CO})$ subunits (Fig. 3*A*), but also escape from the protein and enter the cavities in adjacent $\beta(\text{Ni})$ subunits even at 95 K (Fig. 3*B*). As the same situation is seen with the counterpart hybrid $\text{XL}[\alpha(\text{Ni})\beta(\text{Fe-CO})]_2$ (Fig. 3*C* and *D*), we discuss the invasion of CO into the Ni(II) subunits after the description of the CO migration pathway in the $\beta(\text{Fe-CO})$ subunits of $\text{XL}[\alpha(\text{Ni})\beta(\text{Fe-CO})]_2$.

CO Migration in $\beta(\text{Fe})$ Subunits in the T-State. In $\text{XL}[\alpha(\text{Ni})\beta(\text{Fe-CO})]_2$, the photodissociated CO is clearly observed in $\beta\text{Xe}2$ between helices B and E (Figs. 1*D* and 3*D*), circumscribed by the hydrophobic side chains of $\beta 28\text{Leu}(B10)$, $\beta 67\text{Val}(E11)$, $\beta 68\text{Leu}(E12)$, and $\beta 106\text{Leu}(G8)$. It is likely that the dissociated CO has overcome the $\beta 67\text{Val}(E11)$ barrier to migrate into $\beta\text{Xe}2$ in the back of DP. In our previous crystallographic study on the same T-state hybrid Hbs at 25 K, although most of the dissociated CO remained in DP in each subunit, a weak electron density peak was detected in $\beta\text{Xe}2$, in agreement with our present results.

In $\text{XL}[\alpha(\text{Ni})\beta(\text{Fe-CO})]_2$ at 95 K, another positive electron density feature of CO is present in $\beta\text{Xe}1$ between helix G, helix H, and the β heme (Figs. 3*D* and 4*B*), surrounded by the hydrophobic amino acid side chains of $\beta 71\text{Phe}(E15)$, $\beta 103\text{Phe}(G5)$, $\beta 134\text{Val}(H12)$ and $\beta 137\text{Val}(H15)$ and the vinyl group of heme

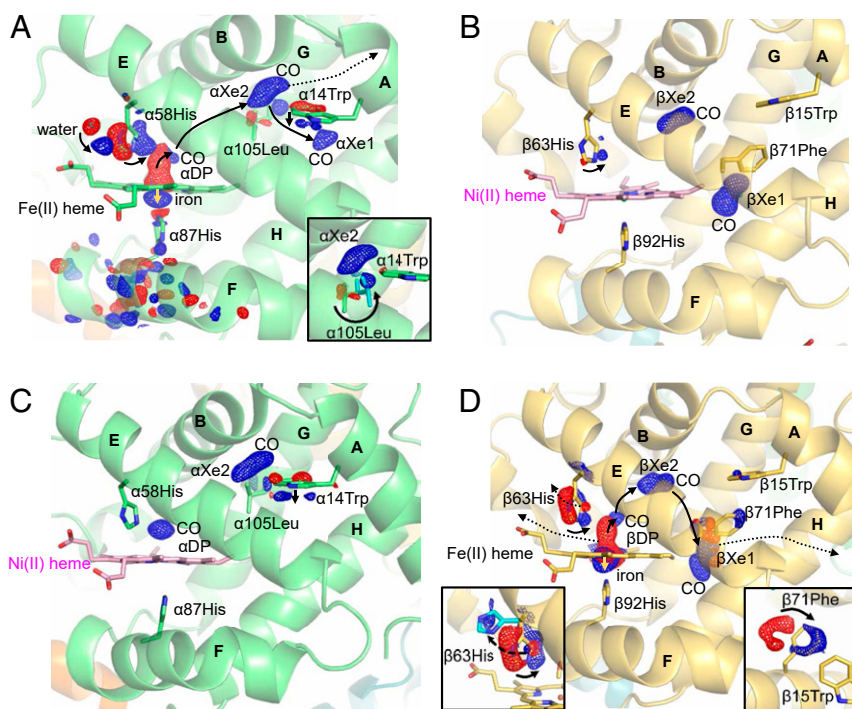


Fig. 3. CO migration in T-state Hb on CO photolysis at 95 K. The datasets are the same as in Fig. 2. (*A* and *B*) Views of $|F_{\text{obs}}^{\text{light}} - |F_{\text{obs}}^{\text{dark}}|$ difference Fourier electron density maps for $\text{XL}[\alpha(\text{Fe-CO})\beta(\text{Ni})]_2$ contoured at $\pm 3.5\sigma$ ($\pm 0.19 \text{ e}/\text{\AA}^3$) for the $\alpha(\text{Fe-CO})$ subunit (*A*) and $\beta(\text{Ni})$ subunit (*B*). (*C* and *D*) Views of $|F_{\text{obs}}^{\text{light}} - |F_{\text{obs}}^{\text{dark}}|$ difference Fourier electron density maps for $\text{XL}[\alpha(\text{Ni})\beta(\text{Fe-CO})]_2$ contoured at $\pm 3.5\sigma$ ($\pm 0.18 \text{ e}/\text{\AA}^3$) for the $\alpha(\text{Ni})$ subunit (*C*) and $\beta(\text{Fe-CO})$ subunit (*D*). In each panel, blue and red indicate positive and negative difference electron density, respectively, and the α and β subunits are shown in green and amber, respectively. The data collected for 60 min after the start of laser irradiation is used for the light structure (*SI Appendix, Table S1*). Some key residues are highlighted with sticks. (*Insets*) Correlated side chain motions of $\alpha 105\text{Leu}(G12)$, $\beta 63\text{His}(E7)$, and $\beta 71\text{Phe}(E15)$ contoured at $\pm 3.5\sigma$ ($\pm 0.19 \text{ e}/\text{\AA}^3$), $\pm 2.5\sigma$ ($\pm 0.13 \text{ e}/\text{\AA}^3$), and $\pm 2.5\sigma$ ($\pm 0.13 \text{ e}/\text{\AA}^3$), respectively.

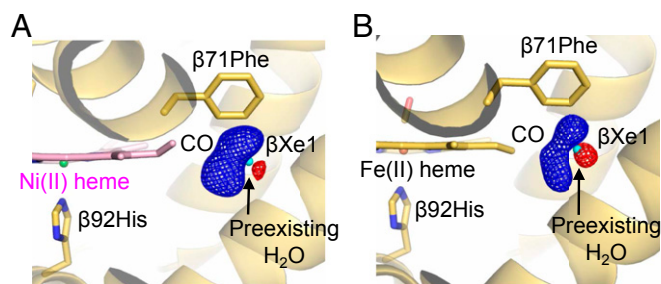


Fig. 4. Photodissociated CO molecules that replace water molecules in the βXe1 sites in β subunits. $|F_{\text{obs}}^{\text{light}} - F_{\text{obs}}^{\text{dark}}|$ difference Fourier electron density maps for T-state $\text{XL}[\alpha(\text{Fe-CO})\beta(\text{Ni})]_2$ (A) and T-state $\text{XL}[\alpha(\text{Ni})\beta(\text{Fe-CO})]_2$ (B) contoured at $\pm 2.5\sigma$ ($\pm 0.14 \text{ e}/\text{\AA}^3$) and $\pm 3.5\sigma$ ($\pm 0.18 \text{ e}/\text{\AA}^3$), respectively. Blue and red indicate positive and negative difference electron density, respectively. Note that the difference electron density profile in each panel can be interpreted as the replacement of the water molecule by a CO molecule but not solely as a change in the position of the preexisting water molecule, because of a net increase in electron density and because of the shape of the positive difference electron density, possibly representing a two-atom molecule (see also *SI Appendix, Fig. S2*).

ring B. This site is very close to the central water-filled cavity of Hb and has been occupied by a water molecule before photolysis, which is displaced by the photodissociated CO (Fig. 4B). The replacement of water with CO results in a dumbbell-shaped positive feature of CO and a weak spherical negative feature of water, as shown in Fig. 4B. Similar electron density features are observed in the counterpart hybrid $\text{XL}[\alpha(\text{Fe-CO})\beta(\text{Ni})]_2$ (Fig. 4A, and *SI Appendix, Fig. S2*). A previous crystallographic study on T-state deoxy Hb under pressurized Xe also reported the replacement of this water by Xe1 in β subunits (6).

Taken together, our results suggest that a likely CO migration pathway within T-state β subunits is $\text{DP} \rightarrow \beta\text{Xe2} \rightarrow \beta\text{Xe1} \rightarrow \text{solvent}$ (Fig. 3D). This pathway agrees well with the MD study, showing that a high percentage of ligand molecules escape via the β -internal tunnel encompassing βXe2 and βXe1 in both T and R (7). The MD simulations also indicate that the open conformation of $\beta 71\text{Phe}(\text{E15})$, which is favored in T and disfavored in R or R2, permits ligands to migrate between βXe1 and the central water-filled cavity of Hb (7). Consistent with this calculation, the $|F_{\text{obs}}^{\text{light}} - F_{\text{obs}}^{\text{dark}}|$ map around $\beta 71\text{Phe}(\text{E15})$ in T-state $\text{XL}[\alpha(\text{Ni})\beta(\text{Fe-CO})]_2$ provides evidence for its sparsely-populated, closed conformation moving to a position of the open conformation on photolysis (Fig. 3D, *Inset*, lower right).

It is important to point out here that the difference Fourier map for T-state $\text{XL}[\alpha(\text{Ni})\beta(\text{Fe-CO})]_2$ suggests a transient occurrence of a swing-out motion of the distal $\beta 63\text{His}(\text{E7})$ on photolysis (Fig. 3D, *Inset*, lower left), although no such motion can be detected for the distal $\alpha 58\text{His}(\text{E7})$ in the counterpart hybrid $\text{XL}[\alpha(\text{Fe-CO})\beta(\text{Ni})]_2$. Our structural analyses on the R and R2 states of Hb provide more evidence of the distal $\alpha 58/\beta 63\text{His}(\text{E7})$ swing-out motion (as described below in more detail), suggesting that at least some CO molecules can escape directly through a transient E7 channel as well as through an internal cavity network.

CO Invasion into Ni(II) Subunits Indicates the High Gas Permeability of the T State. Regarding the CO invasion into Ni(II) subunits, the CO docking sites observed in $\beta(\text{Ni})$ subunits of $\text{XL}[\alpha(\text{Fe-CO})\beta(\text{Ni})]_2$ (Fig. 3B) are very similar to those in $\beta(\text{Fe-CO})$ subunits of the counterpart hybrid $\text{XL}[\alpha(\text{Ni})\beta(\text{Fe-CO})]_2$ (Fig. 3D), confirming the distribution of the photodissociated CO in β subunits of Hb. Similar confirmation can be made for α subunits by comparing the CO docking sites between $\alpha(\text{Fe-CO})$ and $\alpha(\text{Ni})$ subunits (Fig. 3A and C and *SI Appendix, Fig. S1B*). We note here that the dumbbell-shaped electron density in each Ni(II)-subunit cavity (Fig. 3B and C) can be modeled by a CO molecule (*SI*

Appendix, Figs. S1–S3) but not by a chain of two water molecules, because the oxygen atoms of hydrogen-bonded water molecules are too far apart.

To further demonstrate that the changes in electron density in Ni(II) subunits are due mainly to CO and not to a temperature rise caused by laser irradiation of Ni(II) heme, we performed another series of X-ray measurements using the isomorphous T-state crystal of $\text{XL}[\alpha(\text{Ni})\beta(\text{Ni})]_2$, in which all four subunits contain Ni(II) heme and two $\beta 82\text{Lys}(\text{EF6})$ residues are cross-linked by a fumaryl group. For these measurements, data collection and experimental conditions (including temperature, laser irradiation time, crystal size, and resolution) were similar to those for the crystals of $\text{XL}[\alpha(\text{Fe-CO})\beta(\text{Ni})]_2$ and $\text{XL}[\alpha(\text{Ni})\beta(\text{Fe-CO})]_2$ (*SI Appendix, Table S2 and Fig. S4*). The $|F_{\text{obs}}^{\text{light}} - F_{\text{obs}}^{\text{dark}}|$ difference Fourier electron density maps (contoured at similar density levels as in Fig. 3) show no indication of an increase in electron density in any cavities in $\text{XL}[\alpha(\text{Ni})\beta(\text{Ni})]_2$ with laser irradiation (*SI Appendix, Fig. S5A and B*). There is only a negative electron density feature at βXe1 , signifying displacement of the preexisting water molecule. These results, together with the data in Fig. 3, strongly indicate that the photodissociated CO molecules are able to exit from and reenter the protein matrix even at 95 K, demonstrating the high gas permeability and porosity of Hb. Our data also reveal that CO migration is not just a passive diffusion process but is coupled with side chain motions of key residues, such as $\alpha 14\text{Trp}(\text{A12})$, $\alpha 105\text{Leu}(\text{G12})$, $\beta 63\text{His}(\text{E7})$, and $\beta 71\text{Phe}(\text{E15})$ (Fig. 3A and D, *Insets*).

The obvious question is why ligands can migrate between the subunits of Hb even in the frozen glass state at temperatures $< 160 \text{ K}$. While the answer is not yet clear, a recent simulation study suggests that many ligand molecules exit from and enter the protein matrix via the central cavity of Hb without escaping to the bulk solvent (7). The larger central cavity in T is expected to facilitate ligand diffusion between the subunits within the tetramer compared with R/R2. The experiments described below provide additional evidence in support of this expectation.

R- and R2-State Crystals of COHb. We next investigate the CO migration processes in two representative relaxed quaternary structures, R and R2. Recent structural studies using X-ray crystallography (21, 22), NMR (23), and cryo-EM (24) have shown that a fully-liganded Hb exists in an ensemble of relaxed conformations, varying between the R and R2 boundaries. The R and R2 crystals used in this study are those of COHb C [$\beta 6\text{Glu}(\text{A3}) \rightarrow \text{Lys}$] and COHb A (wild type), respectively, both of which are of $\sim 30 \mu\text{m}$ thickness. Mutant Hb C is used because it forms less soluble, more resistant crystals compared with Hb A (25–27) due to the $\beta 6\text{Glu}$ -to- Lys surface mutation, which does not alter the ligand-binding properties of Hb. We recently demonstrated that thin crystals of R-state COHb C are of high diffraction quality and suitable for photolysis experiments (28).

The X-ray diffraction datasets for the R and R2 crystals were collected at 95 K using the same procedures as for the T crystals. Note, however, that CO recombination is much faster in R/R2 than in T (29), so the photoproduct yield of R/R2 was only $\sim 30\%$ under the irradiation conditions used here. Therefore, we carried out additional data collection at 140 K to facilitate CO migration, based on the temperature-dependent CO migration in Mb crystals (30). At both temperatures with (light) and without (dark) laser irradiation, the R and R2 crystals diffracted to 1.40- to 1.60- \AA and 1.60- to 1.70- \AA resolution, respectively (*SI Appendix, Table S1*). As seen in the $|F_{\text{obs}}^{\text{light}} - F_{\text{obs}}^{\text{dark}}|$ difference Fourier maps of R and R2 (Figs. 5 and 6), although the CO photolysis features are weaker in R/R2 than in T, especially in β subunits with faster recombination kinetics than α (15), there are overall similarities among the difference Fourier maps of T, R, and R2, helping us confirm that the electron density features observed in R and R2 likely reflect important aspects of the CO migration processes rather than noise.

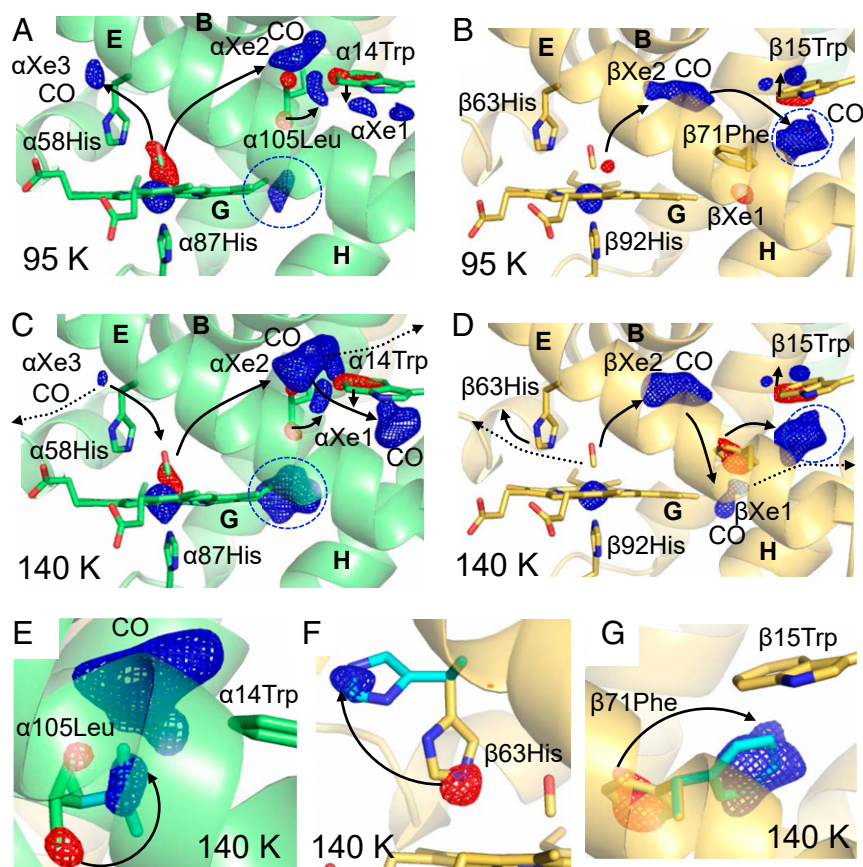


Fig. 5. CO migration in R-state COHb C [β Glu(A3) \rightarrow Lys] on photolysis at 95 and 140 K. (A and B) Views of $|F_{\text{obs}}^{\text{light}} - F_{\text{obs}}^{\text{dark}}|$ difference Fourier electron density maps at 95 K contoured at $\pm 3.0\sigma$ for the α subunit (A) and β subunit (B). (C and D) Views of $|F_{\text{obs}}^{\text{light}} - F_{\text{obs}}^{\text{dark}}|$ difference Fourier electron density maps at 140 K contoured at $\pm 3.0\sigma$ for the α subunit (C) and β subunit (D). (E–G) Correlated side chain motions of key residues at 140 K: α 105Leu(G12) (E), β 63His(E7) (F), and β 71Phe(E15) (G), contoured at $\pm 3.0\sigma$, $\pm 2.4\sigma$, and $\pm 3.0\sigma$, respectively. In each panel, blue and red indicate positive and negative difference electron density, respectively, and the α and β subunits are shown in green and amber, respectively. Blue dotted circles indicate the cavities other than the Xe-binding cavities. The data collected for 60 min after the start of laser irradiation is used for the light structure (SI Appendix, Table S1).

It is important to mention that when the time of laser irradiation was varied from 2 to 60 min at both temperatures, there were no significant changes in the ligand electron density in the cavities of R/R2 (SI Appendix, Table S3 and Figs. S6 to S9), providing no evidence of ligands moving from one site to another with increasing irradiation time. This is in marked contrast to the results obtained with crystals of CO-bound Mb (MbCO), which showed increasing CO density in the Xe-binding cavities with time under illumination with a 532-nm pulsed laser at 100 to 140 K (16). Thus, in the present study, we focus on the temperature-dependent evolution of the electron densities of the photodissociated CO molecules rather than on their time evolution.

CO Migration in the R and R2 States. As expected, in R and R2, the photodissociated CO molecules migrate to more remote sites with increasing temperature. A comparison of Fig. 5A and C and Fig. 6A and C clearly shows that an increase in temperature from 95 K to 140 K decreases the occupancy of CO in α Xe3 close to α DP and lined by the distal α 58His(E7) C β atom but, conversely, increases the CO occupancy in α Xe2. This migration behavior of CO is in line with the MD simulations (7) showing that many of the ligand copies that enter α Xe3 return to α DP (during an early stage of simulation) before migrating to the α internal tunnel encompassing α Xe2 and α Xe1. The simulations estimate that 18% and 33% of the ligand molecules escape to the solvent via α Xe3 in R and R2, respectively, whereas 34% and 10% of escapes occur via α Xe2/ α Xe1 in R and R2, respectively.

As may be expected, CO most likely cannot migrate between the internal cavities and the surrounding bulk solvent at 95 K, which is well below the solvent glass transition temperature (31), even though with laser irradiation the temperature is likely to be slightly higher than that nominally set using a nitrogen gas stream. Such a view may be correct for R/R2 at 95 K (Figs. 5 and 6), but not for T at 95 K, as mentioned above (Fig. 3), suggesting a higher gas permeability of T compared with R/R2. The CO distribution in T-state Hb appears to have already reached equilibrium among subunits at 95 K, with relatively unhindered diffusion of ligands via the larger central cavity. Consequently, the patterns of CO movement in T at 95 K more closely resembles those in R/R2 at 140 K rather than at 95 K.

A further detailed comparison of the difference Fourier maps of T, R, and R2 reveals subtle but important differences among them in terms of the side chain motions of key residues as well as the patterns of CO movement. For example, unlike T with β 71Phe(E15) in its open conformation, in R and R2 this residue adopts a closed conformation, partially capping β Xe1 before and during photolysis at 95 K (Figs. 5B and 6B). This closed conformation expands the volume of a non-Xe-binding cavity below β 15Trp(A12) (blue dotted circles in Figs. 5B and 6B), allowing the entrance of CO at 95 K. Correlated side chain displacement of β 15Trp(A12) is evident in R (Fig. 5B). When the temperature is raised to 140 K, the phenyl ring of β 71Phe(E15) transiently switches to an open conformation (an alternative rotamer, as shown in Fig. 5G), which simultaneously ejects CO from the cavity

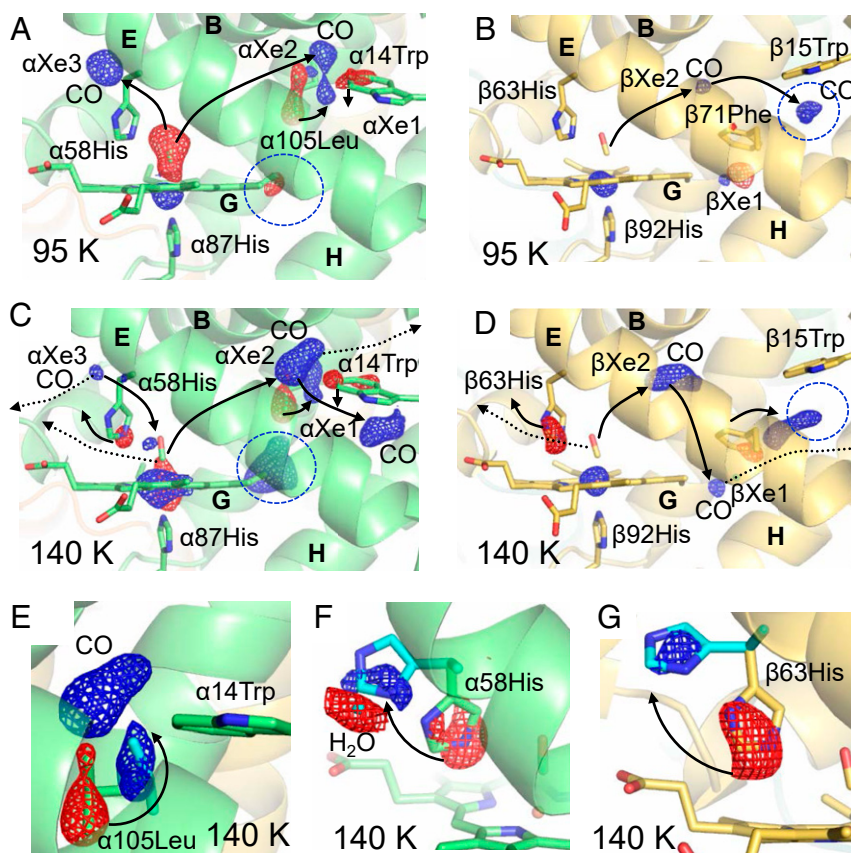


Fig. 6. CO migration in R2-state COHb A on photolysis at 95 and 140 K. (A and B) Views of $|F_{\text{obs}}^{\text{light}} - F_{\text{obs}}^{\text{dark}}|$ difference Fourier electron density maps at 95 K contoured at $\pm 3.0\sigma$ for α subunit (A) and β subunit (B). (C and D) Views of $|F_{\text{obs}}^{\text{light}} - F_{\text{obs}}^{\text{dark}}|$ difference Fourier electron density maps at 140 K contoured at $\pm 3.0\sigma$ for the α subunit (C) and β subunit (D). (E–G) Correlated side chain motions of key residues at 140 K: $\alpha 105\text{Leu(G12)}$ (E), $\alpha 58\text{His(E7)}$ (F), and $\beta 63\text{His(E7)}$ (G), contoured at $\pm 3.0\sigma$, $\pm 2.0\sigma$, and $\pm 2.4\sigma$, respectively. In each panel, blue and red indicate positive and negative difference electron density, respectively, and the α and β subunits are shown in green and amber, respectively. Blue dotted circles indicate the cavities other than the Xe-binding cavities. The data collected for 60 min after the start of laser irradiation is used for the light structure (SI Appendix, Table S1).

below $\beta 15\text{Trp(A12)}$ and permits CO migration from βXe2 to βXe1 (Figs. 5D and 6D) and probably further to the central water-filled cavity of Hb, as suggested by the MD simulations (7). It is interesting to note that previous time-resolved resonance Raman spectroscopic studies on solution COHb found a transient change in the Raman lines of $\alpha 14\text{Trp(A12)}$ and $\beta 15\text{Trp(A12)}$ in a very short time after photolysis (32, 33), which may relate to the observed displacements of these Trp(A12) residues as seen in Figs. 5 and 6.

There is also electron density evidence that the distal His(E7) transiently swings out of DP in both subunits in R2 at 140 K (Fig. 6 F and G) and only in β subunits in R at 140 K (Fig. 5F). No detectable displacements occur at 95 K in R and R2. We speculate that these deligation-induced transient motions of His(E7) are a sign of direct exit of CO from DP to the solvent, supporting the distal His(E7) gate hypothesis (34, 35), in which the ligand entry to and exit from DP is gated by swinging of the imidazole ring of His(E7) out of DP. It should be noted that the movement of the distal His(E7) toward the site occupied by CO is less visible in R/R2 at 140 K (Figs. 5F and 6 F and G) than in T at 95 K (Fig. 3 A and D). This result is consistent with the photolysis-induced structural changes observed at 25 to 35 K (12) and also in line with the view that both liganded and unliganded heme can be accommodated equally well within the more plastic R state (36), as the strain energy retained by the distal His(E7) is much smaller in R/R2 than in T.

In addition, in R and R2, a positive electron density feature appears in a small cavity beside the α heme (blue dotted circles in

Figs. 5A and C and 6C), whereas no electron density is observed in T (Fig. 3A). This site corresponds to the position of βXe1 in β subunits (Fig. 1D). However, the following facts are important to note. Previous studies of the crystal structure of R-state horse deoxy Hb (Protein Data Bank [PDB] ID code 1IBE) (36) showed that one water molecule is located at this cavity in the unliganded R state but not in the CO-liganded R state (PDB ID code 1G0B) (37), suggesting a ligation-linked water molecule displacement in R. Moreover, comparing βXe1 and the α cavity, amino acid differences at the G10 and H16 positions (i.e., $\beta 107\text{Gly[G10]} \rightarrow \alpha 102\text{Ser}$ and $\beta 138\text{Ala[H16]} \rightarrow \alpha 133\text{Ser}$) decrease the size and hydrophobicity of the α cavity, making it less accessible to CO and Xe. Thus, it is likely that the observed electron density beside the α heme in R/R2 is at least partly due to a water molecule entering from the solvent on deligation of the α heme.

Comparison with Related Studies. Our present results suggest that some CO molecules can escape directly through a transient E7 channel in addition to an internal cavity network in all quaternary states T, R, and R2. Consistent with this idea, recent MD simulations by Shadrina et al. (7) showed that an average of 23%, 31%, and 46% of the ligand escaped to the solvent directly from the DP of T, R, and R2, respectively, with the remainder escaping through the interior tunnels. Moreover, previous simulations by Lucas and Guallar (38) have shown an average of 40% and 51% of the ligand escaping from the distal path of T and R2, respectively. Both simulation studies indicated a larger preference for the distal path in β subunits, especially in R2 (7, 38), in agreement with the

present findings. Recent simulations also have suggested an interesting mechanism in which the ligand can escape to the solvent directly from the DP even with the His(E7) gate closed (8). Unfortunately, our data neither support nor directly contradict this mechanism.

A recent room temperature time-resolved X-ray analysis of R-state COHb crystals after photolysis found no electron density of the photodissociated CO in any of the reported Xe cavities (15). This contradiction with the present data on the same R crystals (Fig. 5A–D) is unexplained but possibly could arise from the highly transient and dynamic nature of migrating ligand, making its detection difficult, especially at room temperature. Indeed, although the multiphasic CO geminate rebinding in the R-state COHb crystal at room temperature indicated the existence of at least one CO docking site other than DPs (15), no electron density of CO was found in any of possible sites. The existence of discrete docking sites for the photodissociated CO within Hb has also been demonstrated by a previous kinetics study that found biphasic geminate rebinding of CO to R-state Hb encapsulated in wet silica gels (39).

Finally, we should consider and discuss the lessons learned from studies of the monomeric oxygen storage protein Mb, whose ligand migration mechanism has been extensively investigated using various experimental and simulation techniques. In 1966, Perutz and Matthews (34) proposed that O₂ enters mammalian Hb and Mb by a short, direct channel gated by the distal His(E7) near the solvent edge of the heme. Subsequently, the existence of internal Xe-binding cavities was discovered in the Mb crystal structure (40), leading some researchers to argue that instead of passing through the E7 channel, diatomic gaseous ligands, including O₂ and CO, may enter and exit globins through apolar tunnels involving Xe sites (41). MD simulations have provided theoretical support for this idea (42, 43).

Direct evidence for movement of photodissociated CO molecules into the Xe-binding cavities in Mb comes from X-ray crystallographic studies at room and cryogenic temperatures (13, 14, 16, 30, 44–46). However, the migration of photodissociated CO between the Xe sites in MbCO crystals cannot by itself define the ligand exit pathway, because the ligand exit process involves overcoming activation barriers and the resultant high-energy transition states cannot be observed directly. Kinetic measurements on ligand entry and exit and the lifetimes of the photodissociated states are needed. Scott et al. (35) systematically examined the effects of large-to-small amino acid substitutions on the rates of O₂ entry into and exit from Mb in solution using 90 mutants at 27 different positions and found that mutations at the Xe sites and along the proposed apolar tunnels had little effect on measured rates for ligand entry and exit, although they often affected the geminate kinetics. Time-resolved room temperature X-ray measurements of MbCO crystals after photodissociation of CO showed that the lifetime of CO electron density in the Mb Xe1 cavity (located on the proximal side of the heme pocket) increased dramatically when the size of the B10 side chain (located at the DP wall) was increased (47). These findings indicate that although photodissociated ligands can migrate into the Xe-binding cavities, they must move back to the DP to exit the protein. Since the active site structures and the E7

channels in the subunits of human Hb are similar to those in Mb, we should keep in mind the possibility that, as in Mb, some CO molecules in the internal cavities may return to the DP in Hb. However, there is far less information about the functional role of apolar tunnels in human Hb, and the distal His(E7) channel is not the universal pathway for ligand entry into and exit from all globins (48). Further studies combining X-ray crystallography and mutagenesis as well as MD simulations could improve our understanding of the ligand migration mechanism of human Hb.

Conclusions

Our high-quality electron density maps provide a comprehensive picture of CO migration processes in the T, R, and R2 quaternary structures of human Hb and highlight the relevance of cavities, nonpolar residues, and the distal His(E7) in rapid ligand exit and entry in Hb. Despite a similar folding topology in both subunits of Hb, the photodissociated CO diffuses by hopping between the internal cavities along the pathway in a different direction in each subunit of all quaternary states. The distribution of CO in the cavities depends somewhat on the quaternary state. The side chain of His(E7) also acts as a transient gate for ligand in all quaternary states, although this is less evident in α subunits than in β subunits. In addition to the distal $\alpha 58/\beta 63$ His(E7), $\alpha 14$ Trp(A12), $\alpha 105$ Leu(G12), $\beta 15$ Trp(A12), and $\beta 71$ Phe(E15) are revealed as the key residues controlling ligand migration in each quaternary state of Hb. The present results strongly suggest the existence of multiple ligand migration pathways in both subunits of Hb (7, 37, 39) and emphasize the functional relevance of the high gas permeability and porosity of the T-state Hb molecule (49, 50) in facilitating rapid O₂ diffusion and delivery to the tissues.

Materials and Methods

Detailed information on the materials and methods used in this study, including sample preparation, crystallization, X-ray structural determination, and data collection and refinement statistics, are provided in *SI Appendix*.

Data Availability. Structural data have been deposited in the Protein Data Bank (<https://www.rcsb.org/>) with PDB ID codes 6KA9 for T-state XL[α (Fe-CO) β (Ni)]₂ (dark, 95 K), 6KAE for T-state XL[α (Fe-CO) β (Ni)]₂ (light 60 min, 95 K), 6KAH for T-state XL[α (Ni) β (Fe-CO)]₂ (dark, 95 K), 6KAI for T-state XL[α (Ni) β (Fe-CO)]₂ (light 60 min, 95 K), 6KAO for R-state COHb C (dark, 95 K), 6KAP for R-state COHb C (light 60 min, 95 K), 6KAQ for R-state COHb C (dark, 140 K), 6KAR for R-state COHb C (light 60 min, 140 K), 6KAS for R2-state COHb A (dark, 95 K), 6KAT for R2-state COHb A (light 60 min, 95 K), 6KAU for R2-state COHb A (dark, 140 K), 6KAV for R2-state COHb A (light 60 min, 140 K), 6L5V for R-state COHb C (light 2 min, 95 K), 6L5W for R-state COHb C (light 2 min, 140 K), 6L5X for R2-state COHb A (light 2 min, 95 K), 6L5Y for R2-state COHb A (light 2 min, 140 K), 6LCW for T-state XL[α (Ni) β (Ni)]₂ (dark, 95 K), and 6LCX for T-state XL[α (Ni) β (Ni)]₂ (light 60 min, 95 K) (details in *SI Appendix, Tables S1 to S3*).

ACKNOWLEDGMENTS. We thank the staff members at the NW12A beamline station of the Photon Factory, KEK Tsukuba, for assistance with X-ray data collection. This work was supported by Japan Society for the Promotion of Science KAKENHI Grants JP 16K07326 (to N.S.), JP 17H06372 (to A.S.-T.), JP 19K06601 (to N.S.), and JP 19H05779 (to S.-Y.P.). X-ray data were collected with the approval of the Photon Factory Program Advisory Committee (Proposals 2018G051 and 18S2-002).

1. M. F. Perutz, H. Muirhead, J. M. Cox, L. C. G. Goaman, Three-dimensional Fourier synthesis of horse oxyhaemoglobin at 2.8-Å resolution: The atomic model. *Nature* **219**, 131–139 (1968).
2. J. Monod, J. Wyman, J. P. Changeux, On the nature of allosteric transitions: A plausible model. *J. Mol. Biol.* **12**, 88–118 (1965).
3. R. G. Shulman, J. J. Hopfield, S. Ogawa, Allosteric interpretation of haemoglobin properties. *Q. Rev. Biophys.* **8**, 325–420 (1975).
4. J. Baldwin, C. Chothia, Haemoglobin: The structural changes related to ligand binding and its allosteric mechanism. *J. Mol. Biol.* **129**, 175–220 (1979).
5. M. F. Perutz, Mechanisms of cooperativity and allosteric regulation in proteins. *Q. Rev. Biophys.* **22**, 139–237 (1989).
6. C. Savino et al., Pattern of cavities in globins: The case of human hemoglobin. *Bio-polymers* **91**, 1097–1107 (2009).
7. M. S. Shadrina, G. H. Peslherbe, A. M. English, Quaternary-linked changes in structure and dynamics that modulate O₂ migration within hemoglobin's gas diffusion tunnels. *Biochemistry* **54**, 5268–5278 (2015).
8. M. S. Shadrina, G. H. Peslherbe, A. M. English, O₂ and water migration pathways between the solvent and heme pockets of hemoglobin with open and closed conformations of the distal HisE7. *Biochemistry* **54**, 5279–5289 (2015).
9. I. Birukou, J. Soman, J. S. Olson, Blocking the gate to ligand entry in human hemoglobin. *J. Biol. Chem.* **286**, 10515–10529 (2011).
10. I. Birukou, D. H. Mailliet, A. Birukova, J. S. Olson, Modulating distal cavities in the α and β subunits of human HbA reveals the primary ligand migration pathway. *Biochemistry* **50**, 7361–7374 (2011).
11. W. A. Saffran, Q. H. Gibson, Photodissociation of ligands from heme and heme proteins. Effect of temperature and organic phosphate. *J. Biol. Chem.* **252**, 7955–7958 (1977).

12. S. Adachi, S.-Y. Park, J. R. H. Tame, Y. Shiro, N. Shibayama, Direct observation of photolysis-induced tertiary structural changes in hemoglobin. *Proc. Natl. Acad. Sci. U.S.A.* **100**, 7039–7044 (2003).
13. T.-Y. Teng, V. Srajer, K. Moffat, Photolysis-induced structural changes in single crystals of carbonmonoxy myoglobin at 40 K. *Nat. Struct. Biol.* **1**, 701–705 (1994).
14. I. Schlichting, J. Berendzen, G. N. Phillips, Jr, R. M. Sweet, Crystal structure of photolysed carbonmonoxy-myoglobin. *Nature* **371**, 808–812 (1994).
15. F. Schotte *et al.*, Real-time tracking of CO migration and binding in the α and β subunits of human hemoglobin via 150-ps time-resolved Laue crystallography. *Chem. Phys.* **422**, 98–106 (2013).
16. A. Tomita *et al.*, Visualizing breathing motion of internal cavities in concert with ligand migration in myoglobin. *Proc. Natl. Acad. Sci. U.S.A.* **106**, 2612–2616 (2009).
17. A. Tomita, T. Sato, S. Nozawa, S. Y. Koshihara, S. Adachi, Tracking ligand-migration pathways of carbonmonoxy myoglobin in crystals at cryogenic temperatures. *Acta Crystallogr. A* **66**, 220–228 (2010).
18. N. Shibayama, H. Morimoto, G. Miyazaki, Oxygen equilibrium study and light absorption spectra of Ni(II)-Fe(II) hybrid hemoglobins. *J. Mol. Biol.* **192**, 323–329 (1986).
19. N. Shibayama, H. Morimoto, T. Kitagawa, Properties of chemically modified Ni(II)-Fe(II) hybrid hemoglobins. Ni(II) protoporphyrin IX as a model for a permanent deoxy-heme. *J. Mol. Biol.* **192**, 331–336 (1986).
20. N. Shibayama *et al.*, Oxygen equilibrium properties of highly purified human adult hemoglobin cross-linked between 82 β 1 and 82 β 2 lysyl residues by bis(3,5-dibromosalicyl) fumarate. *Biochemistry* **30**, 8158–8165 (1991).
21. M. K. Safo, M. H. Ahmed, M. S. Ghatge, T. Boyiri, Hemoglobin-ligand binding: Understanding Hb function and allostery on atomic level. *Biochim. Biophys. Acta* **1814**, 797–809 (2011).
22. N. Shibayama, K. Sugiyama, J. R. H. Tame, S. Y. Park, Capturing the hemoglobin allosteric transition in a single crystal form. *J. Am. Chem. Soc.* **136**, 5097–5105 (2014).
23. J. A. Lukin *et al.*, Quaternary structure of hemoglobin in solution. *Proc. Natl. Acad. Sci. U.S.A.* **100**, 517–520 (2003).
24. M. Khoshouei, M. Radjainia, W. Baumeister, R. Danev, Cryo-EM structure of haemoglobin at 3.2 Å determined with the Volta phase plate. *Nat. Commun.* **8**, 16099 (2017).
25. P. M. Fitzgerald, W. E. Love, Structure of deoxy hemoglobin C (beta six Glu replaced by Lys) in two crystal forms. *J. Mol. Biol.* **132**, 603–619 (1979).
26. J. C. Dewan *et al.*, Structure of mutant human carbonmonoxyhemoglobin C (betaE6K) at 2.0-Å resolution. *Acta Crystallogr. D Biol. Crystallogr.* **58**, 2038–2042 (2002).
27. L. N. Patskovska, Y. V. Patskovsky, S. C. Almo, R. E. Hirsch, COHbC and COHbS crystallize in the R2 quaternary state at neutral pH in the presence of PEG 4000. *Acta Crystallogr. D Biol. Crystallogr.* **61**, 566–573 (2005).
28. A. Sato-Tomita, N. Shibayama, Size- and shape-controlled crystallization of hemoglobin for advanced crystallography. *Crystals (Basel)* **7**, 282 (2017).
29. L. P. Murray *et al.*, The effect of quaternary structure on the kinetics of conformational changes and nanosecond geminate rebinding of carbon monoxide to hemoglobin. *Proc. Natl. Acad. Sci. U.S.A.* **85**, 2151–2155 (1988).
30. A. Ostermann, R. Waschipky, F. G. Parak, G. U. Nienhaus, Ligand binding and conformational motions in myoglobin. *Nature* **404**, 205–208 (2000).
31. W. Doster, The protein-solvent glass transition. *Biochim. Biophys. Acta* **1804**, 3–14 (2010).
32. K. R. Rodgers, T. G. Spiro, Nanosecond dynamics of the R \rightarrow T transition in hemoglobin: Ultraviolet Raman studies. *Science* **265**, 1697–1699 (1994).
33. V. Jayaraman, K. R. Rodgers, I. Mukerji, T. G. Spiro, Hemoglobin allostery: Resonance Raman spectroscopy of kinetic intermediates. *Science* **269**, 1843–1848 (1995).
34. M. F. Perutz, F. S. Mathews, An X-ray study of azide methaemoglobin. *J. Mol. Biol.* **21**, 199–202 (1966).
35. E. E. Scott, Q. H. Gibson, J. S. Olson, Mapping the pathways for O₂ entry into and exit from myoglobin. *J. Biol. Chem.* **276**, 5177–5188 (2001).
36. J. Wilson, K. Phillips, B. Luisi, The crystal structure of horse deoxyhaemoglobin trapped in the high-affinity (R) state. *J. Mol. Biol.* **264**, 743–756 (1996).
37. T. C. Mueser, P. H. Rogers, A. Arnone, Interface sliding as illustrated by the multiple quaternary structures of liganded hemoglobin. *Biochemistry* **39**, 15353–15364 (2000).
38. M. F. Lucas, V. Guallar, An atomistic view on human hemoglobin carbon monoxide migration processes. *Biophys. J.* **102**, 887–896 (2012).
39. S. Sottini *et al.*, Geminate rebinding in R-state hemoglobin: Kinetic and computational evidence for multiple hydrophobic pockets. *J. Am. Chem. Soc.* **127**, 17427–17432 (2005).
40. B. P. Schoenborn, Structure of alkaline metmyoglobin-xenon complex. *J. Mol. Biol.* **45**, 297–303 (1969).
41. R. F. Tilton, Jr, I. D. Kuntz, Jr, G. A. Petsko, Cavities in proteins: Structure of a metmyoglobin-xenon complex solved to 1.9 Å. *Biochemistry* **23**, 2849–2857 (1984).
42. R. F. Tilton, Jr, U. C. Singh, I. D. Kuntz, Jr, P. A. Kollman, Protein-ligand dynamics. A 96-picosecond simulation of a myoglobin-xenon complex. *J. Mol. Biol.* **199**, 195–211 (1988).
43. R. Elber, M. Karplus, Enhanced sampling in molecular dynamics: Use of the time-dependent Hartree approximation for a simulation of carbon monoxide diffusion through myoglobin. *J. Am. Chem. Soc.* **112**, 9161–9175 (1990).
44. K. Chu *et al.*, Structure of a ligand-binding intermediate in wild-type carbonmonoxy myoglobin. *Nature* **403**, 921–923 (2000).
45. V. Srajer *et al.*, Protein conformational relaxation and ligand migration in myoglobin: A nanosecond to millisecond molecular movie from time-resolved Laue X-ray diffraction. *Biochemistry* **40**, 13802–13815 (2001).
46. F. Schotte *et al.*, Watching a protein as it functions with 150-ps time-resolved X-ray crystallography. *Science* **300**, 1944–1947 (2003).
47. M. Schmidt *et al.*, Ligand migration pathway and protein dynamics in myoglobin: A time-resolved crystallographic study on L29W MbCO. *Proc. Natl. Acad. Sci. U.S.A.* **102**, 11704–11709 (2005).
48. M. D. Salter *et al.*, Determination of ligand pathways in globins: Apolar tunnels versus polar gates. *J. Biol. Chem.* **287**, 33163–33178 (2012).
49. P. F. Scholander, Oxygen transport through hemoglobin solutions. *Science* **131**, 585–590 (1960).
50. K. H. Keller, S. K. Friedlander, The steady-state transport of oxygen through hemoglobin solutions. *J. Gen. Physiol.* **49**, 663–679 (1966).